



A New Estimate of the Cosmic Star Formation Density from a Radio-selected Sample, and the Contribution of H -dark Galaxies at $z \geq 3$

Andrea Enia^{1,2} , Margherita Talia^{1,2} , Francesca Pozzi^{1,2} , Andrea Cimatti^{1,3} , Ivan Delvecchio⁴ , Gianni Zamorani² , Quirino D’Amato^{1,5} , Laura Bisigello² , Carlotta Gruppioni² , Giulia Rodighiero⁶ , Francesco Calura² , Daniele Dallacasa¹ , Marika Giuliotti⁷ , Luigi Barchiesi¹ , Meriem Behiri⁷ , and Michael Romano^{6,8}

¹ University of Bologna—Department of Physics and Astronomy “Augusto Righi” (DIFA), Via Gobetti 93/2, I-40129, Bologna, Italy; andrea.enia@unibo.it, margherita.talia2@unibo.it

² INAF—Osservatorio di Astrofisica e Scienza dello Spazio, Via Gobetti 93/3, I-40129, Bologna, Italy

³ INAF—Osservatorio Astrofisico di Arcetri, Largo E. Fermi 5, I-50125, Firenze, Italy

⁴ INAF Osservatorio Astronomico di Brera, via Brera 28, I-20121, Milano, Italy

⁵ INAF/IRA, Istituto di Radioastronomia, Via Piero Gobetti 101, I-40129, Bologna, Italy

⁶ University of Padova—Department of Physics and Astronomy “Galileo Galilei”, Vicolo dell’Osservatorio 3, I-35141, Padova, Italy

⁷ SISSA, Via Bonomea 265, I-34136, Trieste, Italy

⁸ INAF—Osservatorio Astronomico di Padova, Vicolo dell’Osservatorio 5, I-35122, Padova, Italy

Received 2021 July 27; revised 2022 January 31; accepted 2022 February 2; published 2022 March 17

Abstract

The star formation rate density (SFRD) history of the universe is well constrained up to redshift $z \sim 2$. At earlier cosmic epochs, the picture has been largely inferred from UV-selected galaxies (e.g., Lyman-break galaxies; LBGs). However, the inferred star formation rates of LBGs strongly depend on the assumed dust extinction correction, which is not well constrained at high z , while observations in the radio domain are not affected by this issue. In this work we measure the SFRD from a 1.4 GHz selected sample of ~ 600 galaxies in the GOODS-N field up to redshift ~ 3.5 . We take into account the contribution of active galactic nuclei from the infrared-radio correlation. We measure the radio luminosity function, fitted with a modified Schechter function, and derive the SFRD. The cosmic SFRD shows an increase up to $z \sim 2$ and then an almost flat plateau up to $z \sim 3.5$. Our SFRD is in agreement with those from other far-IR/radio surveys and a factor 2 higher than those from LBG samples. We also estimate that galaxies lacking a counterpart in the HST/WFC3 H -band (H -dark) make up $\sim 25\%$ of the ϕ -integrated SFRD relative to the full sample at $z \sim 3.2$, and up to 58% relative to LBG samples.

Unified Astronomy Thesaurus concepts: [Galaxy formation \(595\)](#); [Galaxy evolution \(594\)](#); [Star formation \(1569\)](#); [Radio galaxies \(1343\)](#)

1. Introduction

The cosmic history of star formation in the universe is one of the main topics in the field of galaxy formation and evolution. The number of stars formed per year in a unit of cosmological volume (i.e., star formation rate density, SFRD) is now well understood up to redshift 3, when the universe was no more than 3 Gyr old, thanks to a great number of multiwavelength studies gathered in the past 30 yr (see Madau & Dickinson 2014, for an exhaustive review; more recently, Oesch et al. 2018).

Looking backward in time, the SFRD increases by a factor ~ 8 from the present day, reaching a peak at redshift $z \sim 2$, an epoch known as “cosmic noon”. A similar evolution is observed for the black hole accretion rate density, a proxy for galactic nuclear activity, peaking at similar redshift (Boyle & Terlevich 1998; Madau & Dickinson 2014; Delvecchio et al. 2014). The picture becomes less clear at higher redshifts (Casey et al. 2014; Magnelli et al. 2019). Several studies show a steep decline in the SFRD (Bouwens et al. 2015; McLeod et al. 2016; Ishigaki et al. 2018), although this might be a consequence of sample selection, the vast majority being UV-selected sources such as Lyman-break galaxies (LBGs). Studies performed at

longer wavelengths (i.e., radio or submillimeter bands) show a flatter SFRD at $z > 3$ (Gruppioni et al. 2013; Rowan-Robinson et al. 2016; Novak et al. 2017; Gruppioni et al. 2020; but see also Malefahlo et al. 2022), and a full understanding of the intrinsic evolution of SFRD in the young universe is still uncertain.

There are various possible ways to explain this tension. For example, results based on UV-selected sources rely on the adopted dust extinction correction (e.g., Casey et al. 2014) to infer the bolometric star formation rate (SFR), which is not well constrained at high z . Since the first detections with the Submillimetre Common-User Bolometer Array (SCUBA; Hughes et al. 1998), several far-infrared (FIR) to submillimeter surveys (for an exhaustive review, see Casey et al. 2014) revealed the existence of a population of dusty star-forming galaxies (DSFGs), rare in the local universe, but common at high z , with extreme SFRs (up to 10^3 – $10^4 M_{\odot} \text{ yr}^{-1}$) whose dust-obscured component is directly sampled with FIR observations. However, results based on these observations are limited by the achievable sensitivity and large beam of single-dish FIR/submillimeter telescopes (e.g., Herschel; Lutz et al. 2011; or SCUBA; Holland et al. 1999), which make it hard to reach $z > 3$ and properly identify counterparts for the most distant objects. Moreover, higher-resolution surveys performed with interferometers such as NOEMA and ALMA in the millimeter regime currently cover a too small area to map sufficiently large volumes (e.g., Walter et al. 2016; Dunlop et al. 2017; Franco et al. 2018; Hatsukade et al. 2018; Decarli et al. 2019;

Le Fèvre et al. 2020; Béthermin et al. 2020; Faisst et al. 2020; González-López et al. 2020; Casey et al. 2021).

Radio-selected surveys are a way to overcome some of these issues. The high resolving power reached by interferometers such as the Karl G. Jansky Very Large Array (JVLA or VLA) allows resolutions high enough to facilitate the counterpart identification with respect to FIR/submillimeter single-dish observations, overcoming the beam confusion. Once corrected for possible active galactic nucleus (AGN) contamination, the radio frequencies directly sample star formation processes without being affected by dust extinction, as a consequence of the nature of nonthermal radio emission caused by electrons accelerated in the remnants of supernova explosions of massive stars, and free-free continuum emission coming from H II regions. Results obtained with radio-selected samples show a shallower evolution of the SFRD at $z > 2$ (Novak et al. 2017) than inferred from LBGs, similar to what is derived from FIR surveys.

Moreover, LBGs are not the only star-forming population at $z > 2$. It is becoming more and more evident how the information coming from rest-frame UV samples at high redshift likely misses a nonnegligible amount of star formation, occurring in galaxies undetected in optical/UV bands. Previous studies indicate a contribution of these galaxies to the cosmic SFRD equal to 10% of that by LBGs at $z > 3$, which increases to $\sim 25\%$ – 40% at $z > 4.5$ (Williams et al. 2019; Wang et al. 2019; Gruppioni et al. 2020; Talia et al. 2021). These objects, usually referred to as HST-, UV-, or OIR-dark galaxies, have been selected in different ways: serendipitously in deep CO line scan surveys (Williams et al. 2019), in SCUBA surveys (Riechers et al. 2020), via their extreme near-IR color (Wang et al. 2016, 2019), and in continuum FIR (Franco et al. 2018; Yamaguchi et al. 2019; Gruppioni et al. 2020; Manning et al. 2021) or radio (Talia et al. 2021) surveys. A complete census of their physical properties, their contribution to the star formation history of the universe, as well as a proper understanding of the overlap between the different selections is still under debate.

In this work, we make use of deep 1.4 GHz JVLA observations in the Great Observatories Origins Deep Survey field in the Northern hemisphere (GOODS-N) to measure the SFRD evolution up to $z \sim 3.5$. We also identify a sample of high-redshift galaxies undetected in the HST/WFC3 H band (hereafter H -dark) and measure their contribution to the total cosmic SFRD.

The paper is organized as follows. In Section 2 we present the multiwavelength data set considered in this work, with particular focus on the radio 1.4 GHz observations constituting the starting point of our sample. In Section 3 we describe our sample. In Section 4 we present the radio luminosity function, and in Section 5 we derive the SFRD and assess the contribution of the H -dark galaxies at $z \sim 3.5$.

Throughout this work, we give magnitudes in the AB photometric system, adopt a flat Lambda cold dark matter (Λ CDM) cosmology with $H_0 = 67.8 \pm 0.9 \text{ km s}^{-1} \text{ Mpc}^{-1}$ and $\Omega_M = 0.308 \pm 0.012$ (Planck Collaboration et al. 2016), and assume a Chabrier (2003) initial mass function (IMF).

2. Data

In this work we focus on the radio-selected sample in the GOODS-N field and exploit the great wealth of multiwavelength ancillary data available (from X-ray to radio) and their excellent depth. The GOODS-N field (Dickinson et al. 2003a;

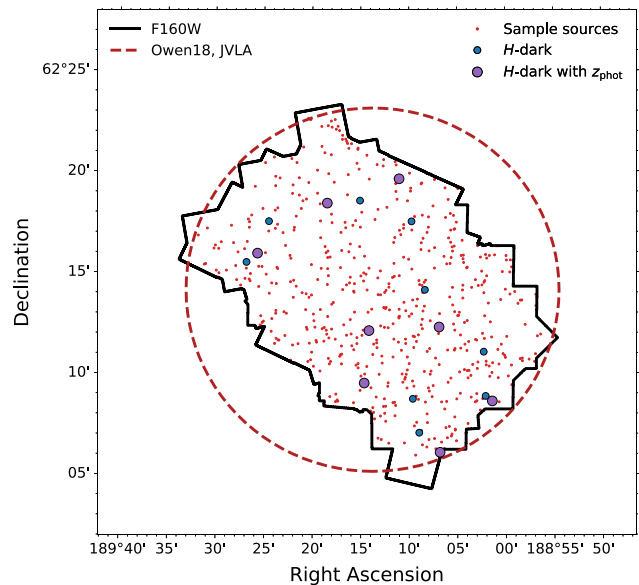


Figure 1. The sample sky coverage. The continuous black line is the HST/WFC3 F160W footprint, while the dashed red circle marks the 1.4 GHz VLA observations in Owen (2018). Red dots are the radio sources studied in this paper, those identified as potentially H -dark are shown in blue, and the purple dots are the sources with photometric redshifts (see Section 5.1 for a note on the H -dark definition).

Giavalisco et al. 2004) is a well-studied portion of the northern sky, overlapping with the Hubble Deep Field North (HDF-N, Williams et al. 1996), centered approximately at R.A. = 12h36m55s, $\delta = 62d14m18s$ and covering an area of $\sim 171 \text{ arcmin}^2$.

2.1. Radio Data

Our starting sample is the 1.4 GHz radio catalog presented in Owen (2018; hereafter O18). We refer to O18 for a complete description of the data analysis and multiband association procedure. Here we summarize the points relevant for the present study.

The map reaches a root-mean-square noise of $2.2 \mu\text{Jy beam}^{-1}$ at the phase center, making it one of the deepest available maps in the radio, at a resolution of $1''.6$. The catalog is extracted from different realizations of the map at varying resolutions ($1''.6$, $2''.0$, $3''.0$, $6''.0$, and $12''.0$), detecting a total of 795 discrete sources down to $5\sigma_{\text{rms}}$ (σ_{rms} changes with the changing resolutions).

The radio observations upon which O18 built their catalog cover an area of $\sim 9'$ radius. However, given the necessity of multiwavelength data, we limited our sample to the footprints of NIR surveys, thus reducing the area of interest for our analysis to 171 arcmin^2 (Figure 1).

In O18, the counterpart identification is based on the deep K_s catalog by Wang et al. (2010; 5σ depth of 24.45), following a criterion based on distance reported in Equation (1) of O18. In the present work, we improve the association process and use a more reliable likelihood procedure instead of a nearest-neighbor method, and search for counterparts in a deeper H -band map (see Section 3.1), down to a 5σ depth of 28.2 mag in the innermost part.

Moreover, we use two additional sets of data in the radio domain in order to measure the radio spectral index α for sources with multiple detections. Guidetti et al. (2017) present

a 5.5 GHz sample of 94 sources (76 of which are also present in our sample) in GOODS-N as part of the eMERGE survey, with a sensitivity of $3 \mu\text{Jy beam}^{-1}$ and $0''.5$ resolution. Murphy et al. (2017) present 10 GHz high-resolution (FWHM $\sim 0''.22$) observations reaching a sensitivity of $5.72 \mu\text{Jy beam}^{-1}$, detecting 32 sources in the field, 22 of which are in our catalog.

2.2. UV-to-FIR Data

The search for counterparts of the radio-selected sources is based on the CANDELS/SHARDS catalog presented in Barro et al. (2019, B19 hereafter), complemented by the super-deblended catalog of Liu et al. (2018) for the FIR photometry (from $24 \mu\text{m}$ to 1.1 mm) and SCUBA-2 observations at $850 \mu\text{m}$ (Cowie et al. 2017).

The catalog from B19 is F160W selected ($1.6 \mu\text{m}$) in the COSMOS and GOODS fields and built by assembling various ancillary multiwavelength observations from the UV to the FIR (Dickinson et al. 2003b; Grogin et al. 2011; Kajisawa et al. 2011; Koekemoer et al. 2011; Ashby et al. 2013, 2015; Hsu et al. 2019). The WFC3 maps were obtained with a stratified (“wedding cake”) observing strategy. The maps reach a detection limit at 5σ of $H = 27.8, 28.2,$ and 28.7 going from the outermost part of the maps to the deep central regions, covering 50%, 15%, and 35% of the total GOODS-N area, respectively. The final B19 catalog in the GOODS-N comprises 35,445 sources.

All the products of B19, including catalogs and maps, are publicly available.⁹ We use the F160W-based catalog for counterpart association and photometry, and the available maps to infer the photometry (or the upper limit rms) of those radio galaxies that are undetected. The B19 sample is constructed by running SEXTRACTOR (Bertin & Arnouts 1996) in dual mode with the F160W catalog as a prior, therefore in shallower bands (e.g., the CFHT *K* band), we end up by having detections for some sources that are fainter than the nominal 5σ limiting magnitude (see Section 3.1 and Table 1).

At wavelengths longer than $8.0 \mu\text{m}$, we do not use the B19 photometry, which is based on a simple cross-matching of Spitzer $24 \mu\text{m}$ (Pérez-González et al. 2005) and Herschel catalogs (Berta et al. 2011; Lutz et al. 2011; Oliver et al. 2012; Magnelli et al. 2013). Instead, our FIR photometry comes from the super-deblended catalog presented in Liu et al. (2018), which uses prior positions from deep Spitzer $24 \mu\text{m}$ and VLA 20 cm data in order to fit the FIR/submm data. As such, Liu et al. (2018) are able to recover more sources by pushing the FIR detections to lower thresholds and Herschel fluxes. Filters from from Spitzer IRS/PUI at $16 \mu\text{m}$ to 1.1 mm observations carried out with AzTEC+MAMBO (whose catalogs are not included in B19) are listed in Table 1. Out of the 2626 sources within the HST/WFC3 footprint, we only keep those with a reported total infrared signal-to-noise ratio (S/N) ≥ 5 ¹⁰, following the advice given by Liu et al. (2018). We also add $850 \mu\text{m}$ fluxes from SCUBA-2 observations (Cowie et al. 2017): 130 radio sources fall within the footprint.

In Table 1 we report a summary of all the bands used throughout this work.

⁹ http://rainbowx.fis.ucm.es/Rainbow_slicer_public

¹⁰ The total infrared S/N is defined as the quadrature sum of the S/Ns measured in all the bands.

Table 1
Summary of All the Filters and Catalogs Considered in This Work

Instrument	Wavelength	Sensitivity (radius $''$)	% of F_{meas}	Reference
KPNO_U	3593 Å	26.7 (1.26)	93.9	(1)
ACS/F435W	4318 Å	27.1 (0.10)	86.5	(1)
ACS/F606W	5915 Å	27.7 (0.10)	94.4	(1)
ACS/F775W	7693 Å	27.2 (0.11)	95.7	(1)
ACS/F814W	0.81 μm	28.1 (0.11)	96.2	(1)
ACS/F850LP	0.90 μm	26.9 (0.11)	96.4	(1)
WFC3/F105W	1.01 μm	26.4 (0.18)	83.2	(1)
WFC3/F125W	1.25 μm	27.5 (0.18)	98.4	(1)
WFC3/F140W	1.39 μm	26.9 (0.18)	69.5	(1)
WFC3/F160W	1.54 μm	27.3 (0.19)	100.0	(1)
MOIRCS Ks	2.13 μm	24.7 (0.60)	67.9	(1)
CFHT K	2.16 μm	24.4 (0.60)	99.6	(1)
IRAC/CH1	3.56 μm	24.5 (1.7)	99.3	(1)
IRAC/CH2	4.51 μm	24.6 (1.7)	99.5	(1)
IRAC/CH3	5.76 μm	22.8 (1.9)	98.4	(1)
IRAC/CH4	8.0 μm	22.7 (2.0)	98.6	(1)
IRS16	16.0 μm	38.5 μJy	78.3	(2)
MIPS24	24.0 μm	26 μJy	84.7	(2)
PACS100	100 μm	1.6 mJy	84.7	(2)
PACS160	160 μm	3.4 mJy	84.7	(2)
SPIRE250	250 μm	7.85 mJy	83.4	(2)
SPIRE350	350 μm	10.35 mJy	69.9	(2)
SPIRE500	500 μm	12.58 mJy	38.4	(2)
SCUBA850	850 μm	1.65 mJy	13.7	(3)
AzTEC	1160 μm	3.3 mJy	29.6	(2)
+MAMBO				
VLA	10 GHz	5.7 $\mu\text{Jy beam}^{-1}$	4.0	(4)
VLA	5.5 GHz	3.0 $\mu\text{Jy beam}^{-1}$	13.5	(5)
VLA	1.4 GHz	2.2 $\mu\text{Jy beam}^{-1}$	100.0	(6)

Note. Sensitivities are given at 5σ ; % of F_{meas} refers to the percentage of the 554 sources identified in the F160W band with a counterpart in the different filters. (1) Barro et al. (2019); 5σ depth computed in apertures with radii reported in Column 3; (2) values derived as 5σ , where σ is the flux uncertainty from Liu et al. (2018); (3) values derived as $5\sigma_s$, where σ_s is the statistical uncertainties from Cowie et al. (2017); i.e., not considering confusion); (4) Guidetti et al. (2017); (5) Murphy et al. (2017); (6) Owen (2018).

2.3. Ancillary Redshifts

B19 provide redshifts for most of the sources presented in their sample. These redshifts fall into the usual categories: z_{spec} for sources with spectroscopic redshift, the great majority coming from Barger et al. (2008), and z_{phot} for sources whose redshifts have been derived from their best-fit spectral energy distribution (SED). The latter category is subsequently divided into three tiers: z_{phot} evaluated with broadband filters only, z_{phot} evaluated with broadband filters plus SHARDS photometry (Pérez-González et al. 2013), and z_{phot} evaluated with broadband filters and/or SHARDS photometry plus WFC3-grism (z_{grism}). These last ones have a reliability flag higher than photometric redshifts, although they are lower than spectroscopic redshifts. In this work, we adopt the B19 z_{spec} and those belonging to the latter category, and reevaluate the remaining z_{phot} .

For two sources we adopt the spectroscopic redshifts of 1.7844 (ID. 386; Decarli et al. 2014) and 1.9200 (ID. 753; Daddi et al. 2015), both measured from multiple submillimeter CO line detections, which we consider more reliable than the previously reported redshifts that were based on the identification of a single emission line in the NIR.

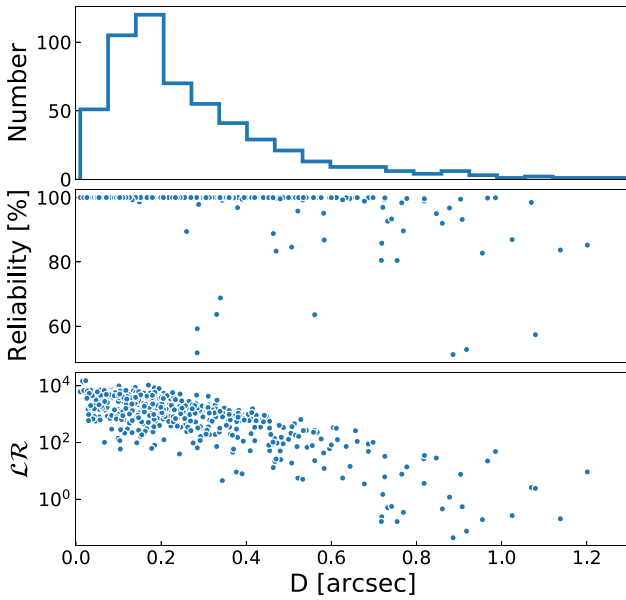


Figure 2. Distribution of the distance between the counterparts chosen through the likelihood ratio from the B19 catalog and our radio sources (upper panel). Also reported are the reliability in percentages (middle panel), and the LR (lower panel).

3. The Sample.

We focus our analysis on the 578 radio sources from the Owen (2018) catalog inside the F160W footprint (see Figure 1), as stated in Section 2.1.

3.1. Counterpart Association

We associate counterparts with the radio sources following the likelihood ratio (LR) technique presented in Ciliegi et al. (2003, 2018). The LR is defined as the ratio of the probability that a given source is the true counterpart and the probability that the same source is an unrelated background object. The choice of one source among the others is expressed in terms of reliability, given as a percentage, as in Equation (5) of Sutherland & Saunders (1992),

$$\text{Rel}_j = \frac{\text{LR}_i}{\sum_i \text{LR}_i + (1 - Q)}, \quad (1)$$

where the i sum is intended over the possible candidate counterparts for each radio source. The source with the highest LR will have the highest reliability, and as such is the associated counterpart.

Starting from our sample of 578 radio sources, within a $1''.6$ radius (equal to the resolution of the radio map), we obtain a reliable association for 548 objects (see Figure 2).

We also use the LR technique to link the radio sources to those in the Liu et al. (2018) and Cowie et al. (2017) catalogs: 560 sources have an FIR association within $2''.0$, and 90 have a SCUBA-2 counterpart within $3''.6$.

For all the 548 radio sources with an associated NIR counterpart, we visually check the cutouts in order to assess the quality of the association, and we correct possible issues. We found that the vast majority of associations are good, but in some cases, we manually fixed them and chose the most likely source by eye. For example, in one case, the radio emission falls exactly between two faint NIR sources, while in another

case, the LR slightly preferred a larger and brighter source at approximately $1''$ over a fainter one whose emission center is almost perfectly coincident with the center of the radio source.

The visual check is similarly performed on the 30 sources without an associated F160W counterpart. In one case, the extended radio emission clearly fell over a strong NIR emission, which is separated by more than $1''.6$ from the center of the radio emission, however. Five objects are very extended low- z sources with the H -band emission center farther than $1''.6$ from the radio emission center. We added these sources to our sample of radio galaxies with an H -band association, which finally contains 554 objects.

As for the remaining 24 sources, in three cases, the radio emission falls clearly on a source that is not present in the B19 catalog either because it lies at the border of the F160W map or due to extreme contamination from a strong nearby source. For another four sources, the radio emission is barely above the 5σ level, either blended into multiple knots of emission or falling in between three NIR sources at $>3''$. These seven sources are conservatively removed from the sample. The residual outcome of the counterpart association and visual check is a group of 17 sources that we call H -dark. Three of them show a marginal detection (below the 3σ level). We point out that the label of H -dark galaxies is not an absolute definition and it clearly depends on the specific depth of the F160W map in the GOODS-N that we are considering in this work.

We search for counterparts to the H -dark galaxies in the IRAC bands by looking at the maps, and we find counterparts for eight out of 17. Five sources are well isolated in the field, with minimal, if any, contamination from nearby sources, therefore we are able to measure their IRAC fluxes with an aperture-corrected photometry of $2''$ radius performed with the PHOTUTILS package of ASTROPY (Bradley et al. 2019). The IRAC emission of the other three galaxies is slightly contaminated by a nearby source, hence the photometry is evaluated with TRACTOR (Lang et al. 2016a, 2016b; Weaver et al. 2022), a PYTHON module for image modeling that uses the known priors on source positions to fit the observed fluxes in multiwavelength bands with a variety of different models, effectively deblending the emissions coming from different sources.

To recapitulate, our final sample consists of 554 sources with an association in the B19 catalog and 17 H -dark sources.

3.2. SED Fitting and Photometric Redshifts

The next step is the characterization of our sources through SED fitting. This is done differently depending on the availability of a reliable spectroscopic redshift or on the necessity of also estimating a photometric redshift.

B19 provide redshifts for every source in their catalog, either coming from a number of different spectroscopic surveys (z_{spec}) or from an SED-fitting evaluated photometric redshift (z_{phot}). Of the 554 radio sources with an NIR counterpart, 392 ($\sim 70\%$) have a reliable spectroscopic redshift, and the remaining 162 ($\sim 30\%$) have a photometric redshift.

The photometric redshift evaluation in B19 is done using six different codes (EAZY, HYPERZ, SPEEDYMC, LEPHARE, ZPHOT, WIKZ) and taking the median of the multiple photo- z estimates as the best-fit value. We note that these codes use galaxy emission models extending up to mid-IR photometry. As reported in Section 2, out of the three tiers of photometric redshifts, we keep those estimated also with WFC3-grism data

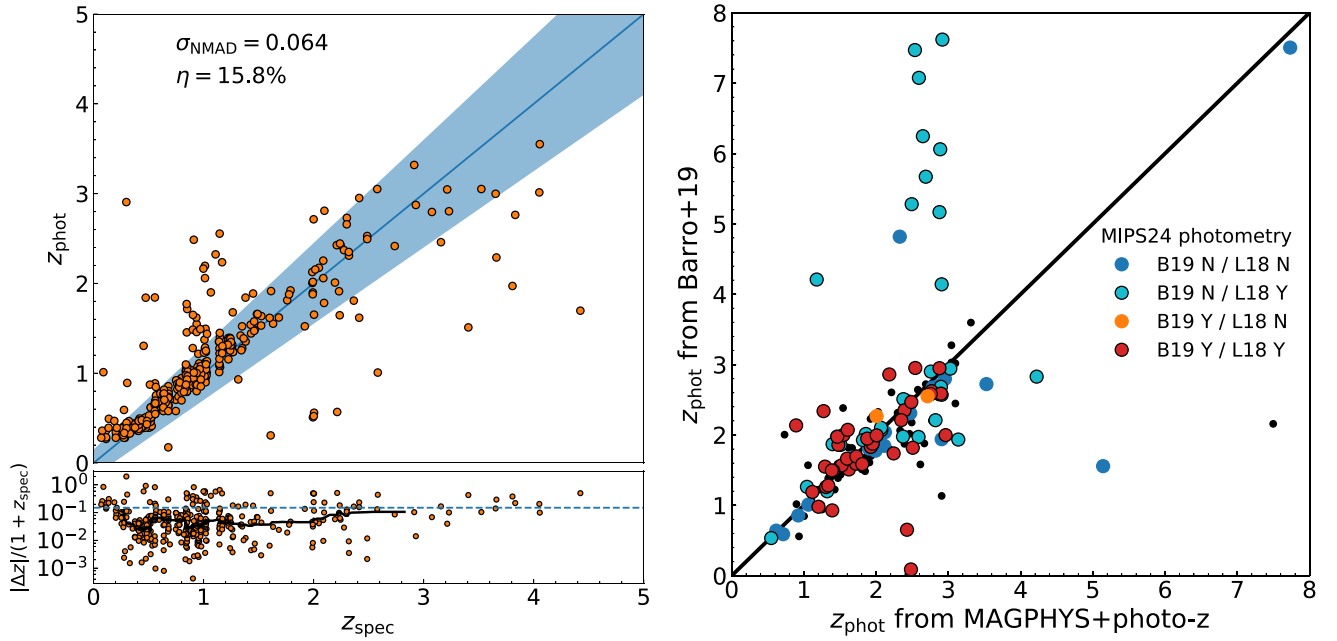


Figure 3. Left panel: comparison between z_{spec} as reported in B19 and z_{phot} evaluated with MAGPHYS + PHOTOF. σ_{NMAD} is the normalized median absolute deviation of the distribution, while η is the fraction of outliers (defined as the sources with $\eta = |\Delta z|/(1 + z_{\text{spec}}) > 0.15$), above the dotted blue line in the bottom panel and outside the blue shading around the 1:1 relation in the top panel. The black line is the running median. Right panel: comparison between the z_{phot} reported in B19 and the z_{phot} evaluated with MAGPHYS + PHOTOF for the 90 sources for which we reevaluated the redshift. The presence (red/orange) or absence (blue/cyan) of FIR photometry in the B19 catalog is highlighted with different colors, while the presence in our catalog (taken from Liu et al. 2018, L18) is highlighted with a marker border. There is a good agreement between the two redshifts, with only 14/90 ($\sim 16\%$) of outliers, the vast majority belonging to sources without FIR in B19. We also show (small black points) the 72 sources labeled z_{grism} (for which we adopt the B19 redshift) in order to illustrate the comparison with MAGPHYS + PHOTOF.

and reevaluate the photometric redshifts for the remaining 90 sources. We use only the broadband photometry, but also add the FIR photometry from the super-deblended catalog.

The photo- z measurement procedure is performed using the MAGPHYS + PHOTOF code (da Cunha et al. 2015; Battisti et al. 2019). MAGPHYS models the emission in the entire UV-to-FIR range assuming that the energy output is balanced between the emission at UV-to-NIR wavelengths and the one absorbed by dust and then reemitted in the FIR. It follows a Bayesian approach to measure the posterior distribution functions (PDF) of the parameters, fitting the observed photometry to a set of galaxy emission models coming from native libraries, composed of 50,000 stellar population spectra with $\psi(t) \propto \exp^{-\gamma t}$ star formation histories with superimposed random bursts (Bruzual & Charlot 2003), associated via the energy balance criterion to 50,000 dust emission SEDs with two components at different temperature (Charlot & Fall 2000; da Cunha et al. 2008). In the MAGPHYS + PHOTOF extension, the code displaces these models in a wide grid of redshifts to infer the PDF of the galaxy photo- z .

In the cases of nondetections, we choose to adopt $3 \times \text{rms}$ as upper limits in order to allow the code to explore the SED model space more freely. We stress that the MAGPHYS does not force the SED model to stay strictly below the limit, instead, it treats the upper limits as values with zero flux and an error equal to the upper limit value (see Section 4.2.3 in the MAGPHYS + PHOTOF documentation). We also verified that there is no significant difference in the photo- z values obtained by adopting $1 \times \text{rms}$ upper limits instead of $3 \times \text{rms}$.

In order to take into account the possible presence of nuclear activity, which could give a nonnegligible contribution to the SED and bias the radio luminosity, we also use SED3FIT

(Berta et al. 2013), which is a MAGPHYS-inspired SED-fitting code, accounting for mid-IR emission possibly coming from the dusty torus of an AGN (Feltre et al. 2012). Since SED3FIT does not implement photometric redshifts measurement, we fix it to those coming from MAGPHYS + PHOTOF for the sources for which we reevaluate it.

A quality assessment of MAGPHYS photo- z is done by measuring photometric redshifts for the subsample of galaxies with available z_{spec} and looking at the outlier fraction of the spectroscopic versus photometric distribution, shown in the left panel of Figure 3.

In the right panel of Figure 3 we compare the photometric redshifts of B19 to those obtained with MAGPHYS + PHOTOF for the first two tiers of redshift reported in B19 (i.e., without the z_{grism} , 90 objects). Not every source in B19 has MIPS photometry at $24 \mu\text{m}$, while we have a full FIR photometry taken from the super-deblended catalog from Liu et al. (2018). As such, we highlight the presence (or lack) of FIR data using different colors and marker edge colors. There is a general agreement between the two redshifts, with a fraction of outliers around 16% of the sample. All but two of the outliers are sources for which we have FIR photometry from the super-deblended catalog and B19 do not. The presence of photometric measurements in the mid-IR (in particular the IRS16 and MIPS24 channels sampling the emission of polycyclic aromatic hydrocarbons) likely allows us to obtain a better constraint for photo- z . We note that our photometric redshifts are in good agreement with those that we label grism-based redshift.

We also apply the described SED-fitting procedure to the eight H -dark galaxies with an associated IRAC emission. At wavelengths shorter than IRAC1, as done for the rest of the

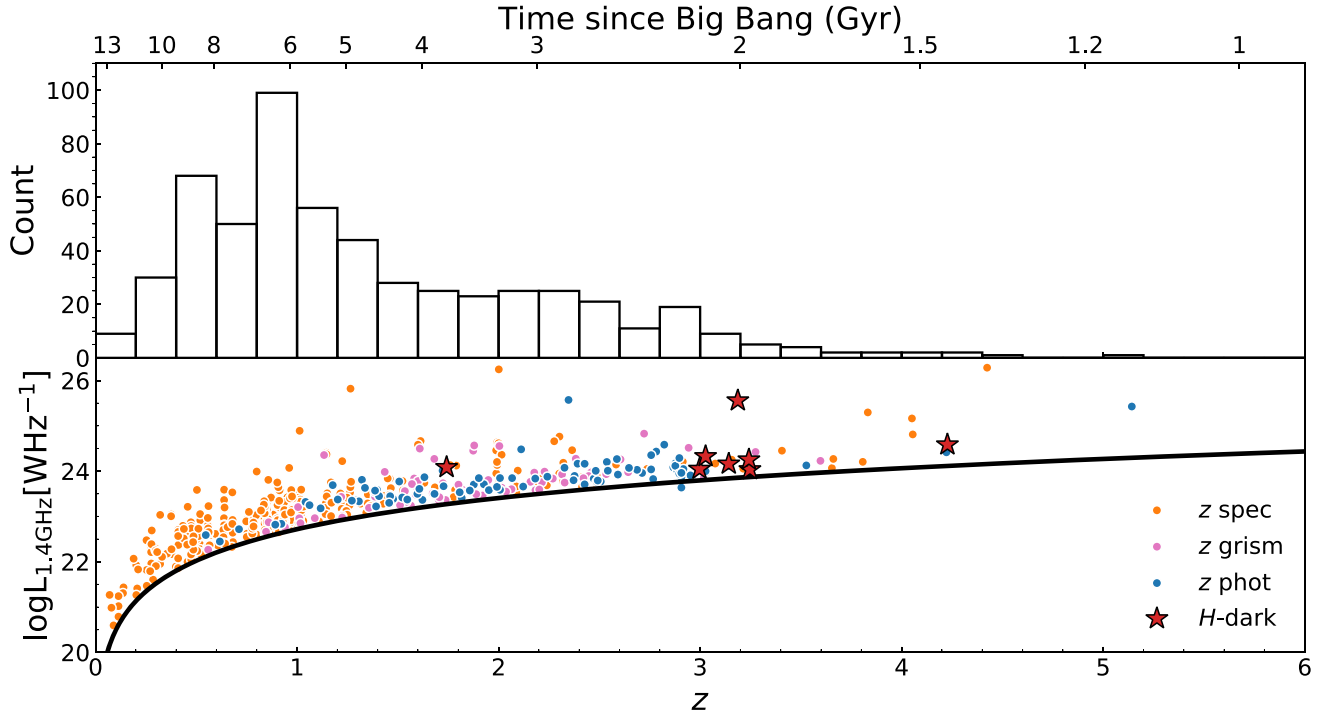


Figure 4. The redshift distribution of the sample (top panel) and rest-frame 1.4 GHz luminosity (bottom panel). Sources are color-coded per redshift type, spectroscopic (orange), grism (pink), and photometric (blue). *H*-dark galaxies are highlighted with red stars. The black line is the 5σ detection limit obtained from the survey flux limit at the best-resolution image of $2.2 \mu\text{Jy beam}^{-1}$ and a fixed spectral slope of $\alpha = -0.7$.

sample, we assume as upper limits $3 \times \text{rms}$, measured directly on the maps, with the exceptions of two sources for which K_s photometry is available.

The best-fit photometric redshifts of the *H*-dark galaxies lie in the $3.00 < z_{\text{phot}} < 3.25$ range, with the exception of one source at $z = 1.74$ and one at $z = 4.23$, the latter showing a quite broad z -PDF (see Figure 11 in the Appendix).

As for the remaining nine *H*-dark sources, the photometry is either not sufficient or is too heavily contaminated by nearby sources to construct a robust SED and estimate a photometric redshift.

In Figure 4 we show the redshift distribution of our sample.

4. The 1.4 GHz Luminosity Function

In order to measure the evolution of cosmic star formation and place constraints on the contributions of the different populations, we first need to estimate the statistical properties of our sample per unit of universe comoving volume.

The radio luminosity function (LF, ϕ) is defined as the number density of radio sources in a given volume of universe per luminosity bin. When measured in different redshift bins, the LF gives information about the density and luminosity evolution of the sources from which it is built. The conjunction of known relations between the luminosities and physical properties (e.g., $L \rightarrow SFR$) with its integration in a certain luminosity range returns insight into processes such as the star formation at a given cosmic epoch.

Our sample redshifts extend to $z \sim 4.5$. In principle, there is a source (ID.424) at $z_{\text{phot}} \sim 7.7$, but we exclude it from the LF evaluation because a single source is not representative of the physical condition of the universe at those extremely high z .

Starting from the assumption that the radio emission follows a simple power law $S_\nu = \nu^\alpha$ and that therefore the radio K

correction is $K(z) = (1+z)^{-(1+\alpha)}$, the final expression for the radio luminosity L at rest-frame frequency of 1.4 GHz derived from the observed flux density S_ν can be written as

$$L_{1.4 \text{ GHz}} = \frac{4\pi D_L^2(z)}{(1+z)^{1+\alpha}} S_\nu, \quad (2)$$

with D_L being the luminosity distance at source redshift z .

There are 79 sources in our sample for which 5 GHz (Guidetti et al. 2017) and/or 10 GHz (Murphy et al. 2017) data exist (57 only have 5 GHz, 3 only 10 GHz, and 19 have both 10 GHz and 5 GHz data), allowing a measurement of the power-law index. Their distribution is shown in Figure 5, with a median value of -0.73 and a dispersion of 0.41, consistent with the value of -0.7 usually adopted in the literature (i.e., Novak et al. 2017). Taking this into account, we fix the power-law index to -0.7 for the sources for which we were unable to measure it directly.

The number counts and the rest-frame 1.4 GHz luminosity, color-coded per redshift type, are shown in Figure 4.

4.1. Completeness Correction and Sample Fidelity

In order to estimate the incompleteness of our sample, we inject artificial sources in simulated maps and look at the fraction of recovered sources as a function of the flux (e.g., Smolčić et al. 2017; Retana-Montenegro et al. 2018; Béthermin et al. 2020).

We simulate multiple VLA observations of the same field, reaching the same noise level as the real observation, therefore assuming that the statistical properties of all the maps are the same. Into each simulation, we inject ~ 2000 sources, separated by at least two times the beam size, whose fluxes are distributed as the observed source counts extrapolated (with a power law)

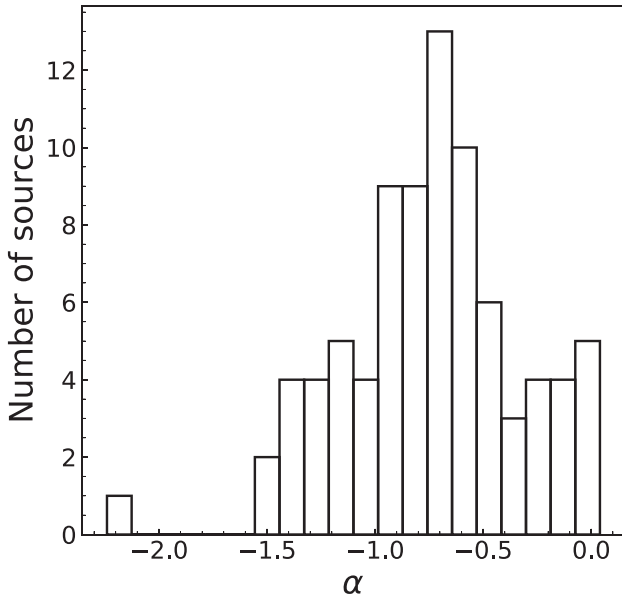


Figure 5. Best-fit radio spectral index α for the 76 galaxies with multiple detections in Murphy et al. (2017), Guidetti et al. (2017), and Owen (2018). The median value is -0.73 , and the 1σ dispersion is 0.42 . For the rest of the sample, we assume a spectral slope of -0.7 .

down to a flux density of $5 \mu\text{Jy}$, thus allowing us to investigate the detectability of sources below the 5σ level. Source sizes come from a fit to the total-to-peak flux ratio S_t/S_p :

$$\frac{S_t}{S_p} = \frac{\sqrt{\theta_M^2 + \theta_b^2} \sqrt{\theta_m^2 + \theta_b^2}}{\theta_b^2}, \quad (3)$$

with θ_M and θ_m being the intrinsic source major and minor FWHM angular sizes, and θ_b the beam FWHM. The simulated sources are built in order to mimic the observed relations between S_p , S_t/S_p , and θ_M (therefore θ_m as previously shown) in the various beam regimes from which the sample is extracted ($\theta = 1''.6, 2''.0, 3''.0, 6''.0, \text{ and } 12''.0$; see Section 2).

The injection is carried out directly on the visibilities in order to take into account effects of the imaging process of bright sources, i.e., side lobes. Source extraction, and therefore the detection fraction, is done with the Python Blob Detector and Source Finder (PyBDSF), which uses the same Gaussian component fit and removal of the task SAD of AIPS used in O18 to build the catalog of detected sources. In accordance with the O18 method of catalog construction, we repeat the source extraction in multiple realizations of the same map, degraded to beams of $2''.0, 3''.0, 6''.0, \text{ and } 12''.0$. We checked that in the simulated sample the S_t/S_p ratios are consistent with those coming from the observed sample, as a Kolmogorov–Smirnov test applied on both shows that they are not generated from the different distributions. This also holds when the samples are divided into two regimes of high ($S_t > 40 \mu\text{Jy}$) and low flux ($S_t < 40 \mu\text{Jy}$).

The results are shown in the top panel of Figure 6, with the detection fraction reported as a function of S/N. The solid blue line is the detection fraction measured for the full sample, while the dashed green and red lines refer to the extended and the circular (i.e., unresolved) parts of the simulations, respectively. We assume that the sample is complete for S/N higher than 20 (fluxes higher than $\sim 40 \mu\text{Jy}$), and we choose to limit our

analysis to a completeness over 50% in order to avoid overcompensating for sources in completeness regimes where we would risk to correct for more sources than are actually observed. This translates into an integrated S/N > 5.20 for unresolved sources and > 7.68 for resolved ones.

We also perform a fidelity analysis on the sample. Fidelity is a function of S/N, and it represents how much we can rely on the assumption that a source with a certain S/N is actually a real detection and not a noise artifact. Following the approach of Decarli et al. (2016), we define the fidelity of a source at a given S/N as

$$f(S/N) = 1 - \frac{N_{\text{neg}}}{N_{\text{pos}}}. \quad (4)$$

N_{neg} is the number of negative detections, that is, the number of detections in the inverse of the simulated maps, and as such a proxy for all the blobs of pure noise that are mistakenly assumed as a good detection. In this way, we are able to estimate the percentage of false detections at any given value of S/N. We limit our analysis to the regimes where the fidelity is higher than 90%, with S/N > 5.20 .

In Figure 7 we show the S/Ns for the 17 H -dark sources: all but two have 1.4 GHz S/N where the fidelity of the sample is over 90%, and 14 of them belong to an S/N regime where the fidelity is 100% (S/N > 6). As such, we trust our sample of H -dark sources to be real with a high degree of confidence.

The S/N cuts reduce the pool of available sources to 479, i.e., 323 with z_{spec} , 65 with z_{grism} , 76 with z_{phot} , and 15 H -dark sources, including the 8 sources with a measure of z_{phot} . The LF analysis in the following section is derived considering this final selection.

4.2. Estimating the AGN Contamination

Samples of radio-selected sources do not include only purely star-forming galaxies because a fraction of their radio luminosities might be associated with nuclear activity. Disentangling the possible AGN contribution to the radio emission is necessary in order to properly convert luminosities into SFRs.

This is usually achieved by conservatively removing the sources showing an excess in their 1.4 GHz emission due to nuclear activity (radio-excess sources; e.g., Novak et al. 2017). While this approach is successful in minimizing the AGN contamination, it completely removes from the sample star formation emission that could in principle be recovered if it were disentangled from the AGN emission. In this work we tried to recover part of these sources by estimating the fraction of radio emission due to AGN (f_{AGN}) and correcting the fluxes accordingly.

Measuring how an AGN can contribute to the radio emission goes through the well-known IR-radio correlation (IRRC; van der Kruit 1971; de Jong et al. 1985; Helou et al. 1985). The IRRC is a tight correlation with a dispersion σ around 0.16–0.22 dex (Delvecchio et al. 2017; Molnar et al. 2021), linking the radio luminosity to the IR luminosity via the ratio

$$q_{\text{TIR}} = \log \frac{L_{\text{IR}}[\text{W}]}{3.75 \times 10^{12}[\text{Hz}]} - \log \frac{L_{1.4\text{GHz}}}{[\text{W Hz}^{-1}]}, \quad (5)$$

where $3.75 \times 10^{12}[\text{Hz}]$ is the central frequency in the wavelength rest-frame 42–122 μm domain. In measuring q_{TIR} (and all the other related quantities), we use the AGN-removed IR luminosity provided by SED3FIT. With SED3FIT, we found a

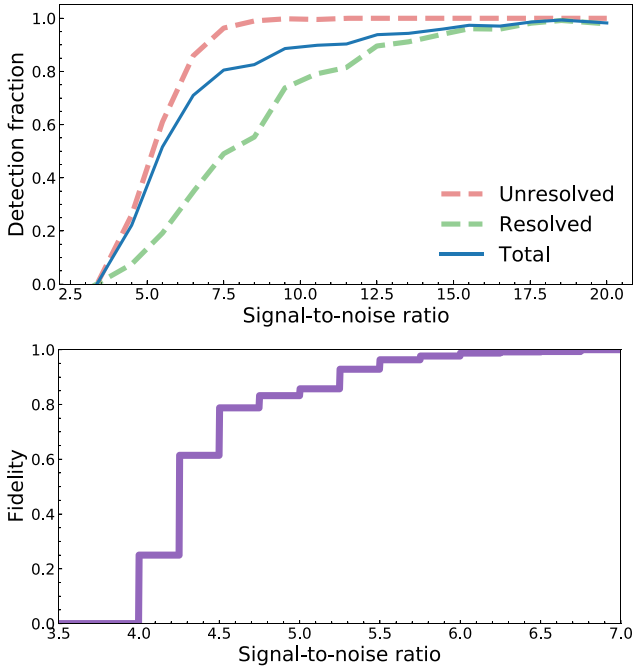


Figure 6. The sample detection fraction (upper panel) and fidelity (lower panel), both obtained from simulations with injected sources of known flux. Upper panel: the blue line is the detection fraction for the full sample, while dashed green and red lines are for the resolved and unresolved injected sources, respectively. Lower panel: the purple step function is the sample fidelity as a function of S/N.

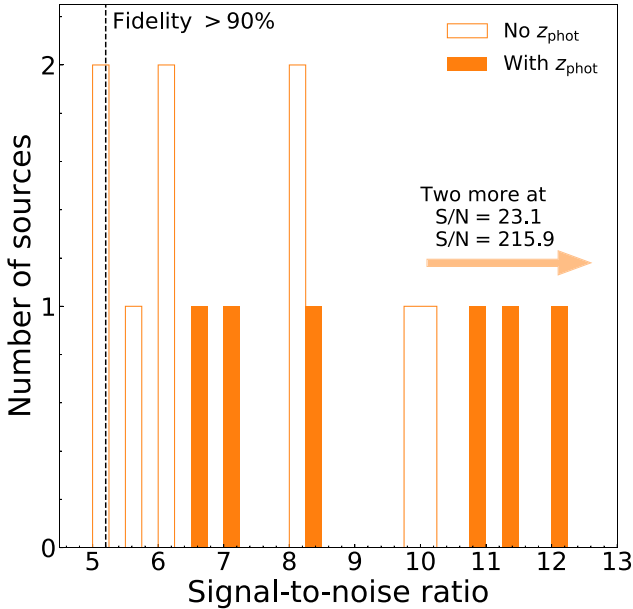


Figure 7. Signal-to-noise ratios at 1.4 GHz for the sample of 17 *H*-dark sources. Sources with $S/N > 5.2$ have a fidelity greater than 90% (see Section 4.1). Filled bars are for the sources with measured z_{phot} .

median mid-IR AGN fraction¹¹ of 16% for the subsample of 81 galaxies with more than 5% mid-IR AGN fraction, 12 of which over 50%.

¹¹ This fraction should not be confused with the f_{AGN} cited earlier, which is the fraction of AGN emission at 1.4 GHz.

Radio emission is the combination of free-free emission from H II regions along with a major contribution of nonthermal emission coming from shock wave acceleration of relativistic electrons produced in supernova explosions of massive stars, whereas the IR comes from the photon reemission of dust heated by similarly massive OB stars, with the electrons experiencing different cooling processes (i.e., bremsstrahlung and inverse Compton scattering) in the host galaxies. The correlation holds in different environments (merging or isolated galaxies; Condon et al. 1993, 2002; Murphy 2013) and over at least three orders of magnitude of the luminosities (e.g., Helou et al. 1985; Condon 1992; Yun et al. 2001).

Here, we use the IRRC, more specifically, the offset from the IRRC, as a way to weight the AGN contribution in the radio (Donley et al. 2005; Del Moro et al. 2013; Bonzini et al. 2015). Delvecchio et al. (2017) studied a sample of 7700 COSMOS radio sources, deriving an analytical expression for a (weakly redshift-dependent) 3σ threshold for sources dominated by AGN emission:

$$r = \log \frac{L_{1.4\text{GHz}} [\text{W Hz}^{-1}]}{\text{SFR}_{\text{IR, SF}} [M_{\odot} \text{yr}^{-1}]} > 22 \times (1+z)^{0.0013}. \quad (6)$$

Sources above this ratio show a radio emission in excess with respect to the one that is compatible with a pure star formation processes. This criterion does not exclude all the possible AGN sources in a sample, but significantly reduces the number of those whose emission is dominated by nuclear processes. Based on this criterion, there are 109 radio-excess sources in our full sample ($\sim 20\%$), 3 of which are *H*-dark objects.

More recently, Delvecchio et al. (2021) calibrated the IRRC considering both time and host stellar mass evolution, finding a strong correlation with M_* and a much weaker one with z , as in Delvecchio et al. (2017), suggesting that the often recovered q_{TIR} evolution with time is more a consequence of the detection of galaxies at lower M_* in the lower redshift bins than a real evolutionary feature.

Ceraj et al. (2018) built their radio AGN LF by measuring the fraction of AGN emission for each object from the IRRC and correcting the observed radio emission accordingly with the measured f_{AGN} . We apply the same method to disentangle the AGN emission from the emission expected from the IRRC due to star-forming processes. We divide our sample into seven redshift bins, locate the peak of q_{TIR} for each bin distribution (\bar{q}_{SF}), mirror the right side of the distribution, and fit the result with a Gaussian to obtain the bin error. We measure the AGN fraction as the difference between the galaxy’s own q_{TIR} and the distribution peak in the appropriate redshift bin $f_{\text{AGN}} = 1 - 10^{q_{\text{TIR}} - \bar{q}_{\text{SF}}}$. We then fit the \bar{q}_{SF} values to infer the evolution of q_{TIR} with $(1+z)$, obtaining a weak trend with redshift that is almost compatible with no evolution at all (-0.09 ± 0.07).

By multiplying the 1.4 GHz luminosities per the measured f_{AGN} , we are making the assumption that the radio emission due to star formation processes should in fact lie exactly on the IRRC. In our sample, we identified 109 radio-excess galaxies. We completely remove from the subsequent analysis 19 AGN-dominated sources ($f_{\text{AGN}} > 95\%$). We also discard 44 galaxies that fall below the 5σ detection threshold after the f_{AGN} correction because they would have not have been detected without the flux boosting due to the AGN presence. In the end,

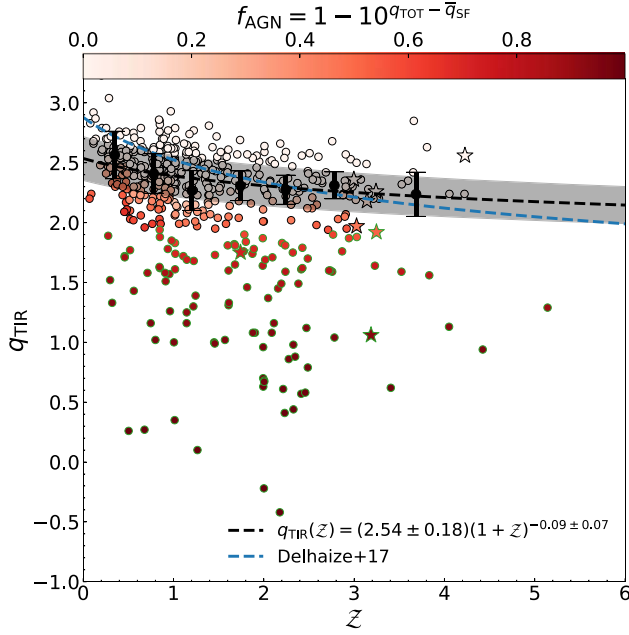


Figure 8. The IRRC for our sample as a function of redshift, color-coded for f_{AGN} . Black circles are measured in bins of z , evaluated as reported in the text, and the best-fit relation (dotted black line) is reported in the legend, while the dotted blue line is the Delhaize et al. (2017) relation. Galaxies plotted with an outer green circle are classified as radio-excess sources following the criterion of Delvecchio et al. (2017). Stars identify the H -dark sources.

we retain 46 radio-excess sources, corrected for f_{AGN} . The results are shown in Figure 8.

Finally, we point out that the results obtained by removing the radio-excess sources from the sample are consistent with those obtained from the f_{AGN} -corrected sample. This is expected because the total fraction of recovered AGNs that does not fall below the map sensitivity limits is $\sim 9\%$ of the sample, which is not enough to translate into a systematic offset in the results. As mentioned at the beginning of this section, in this work, we report the results obtained from the f_{AGN} -corrected sample.

4.3. $1/V_{\text{max}}$ Method and Fit

The 1.4 GHz radio LF is evaluated with the $1/V_{\text{max}}$ method (Schmidt 1968), a nonparametric approach that computes $\phi(L, z)$ measuring the source density from their maximum observable comoving volume, thus being completely independent from any analytical preassumption. The sum is performed on the sources falling within a certain redshift and luminosity bin, divided by the logarithmic bin width $\Delta \log L$:

$$\phi(L, z) = \frac{1}{\Delta \log L} \sum_i \frac{1}{V_{\text{max}}} \quad (7)$$

V_{max} is the maximum observable comoving volume of the universe for the i -th source and is measured as the volume slice between the z_{min} of the redshift bin and the minimum volume between the bin z_{max} and the redshift at which the source becomes undetectable given the survey depth.

We consider the 472 sources with a measured redshift and a fidelity higher than 90% (including the eight H -dark galaxies with photo- z ; see Section 4.1).

Due to the specifics of the O18 sample construction, the survey depth varies in the five map realizations with different

beams from which the sources are extracted due to the different map noises. As such, we assign the proper detection limit to each source of the sample depending on the resolution map in which the source is detected. Sources falling below this limit are excluded from the LF evaluation, i.e., 44 radio-excess sources with f_{AGN} -corrected luminosities.

We compute V_{max} by summing spherical shells in steps of $\Delta z = 0.01$ in the interval between z_{min} and z_{max} while correcting for the different biases affecting the sample:

$$V_{\text{max}} = \sum_{z=z_{\text{min}}}^{z_{\text{max}}} (V(z + \Delta z) - V(z)) \times C_A C_I [S_{1.4\text{GHz}}(z)], \quad (8)$$

where C_A corrects for the survey observed area of 171 arcmin²:

$$C_A = \frac{A_{\text{survey}}}{41253 \text{ deg}^2}, \quad (9)$$

and $C_I [S_{1.4\text{GHz}}(z)]$ is a statistical correction factor varying with the source flux as it moves through the redshifts, parameterizing the survey incompleteness (see Section 4.1).

As in Novak et al. (2017), sources with $\log L$ under the best-resolution detection limit at the bin z_{max} (black curve in Figure 4) are binned in a single luminosity bin, reducing the statistical impact of incompleteness in the faint-end part of the LF. The subsequent bins are equally separated into $\log L$, with the exception of the last redshift bin, where due to the small number of sources, we use bins containing almost the same number of sources.

In order to take into account the uncertainties on the ~ 150 sources with photometric or grism redshift and the more general uncertainty on the radio luminosities, we measure the luminosity function for 1000 different realizations of z and $\log L$, extracted from their probability density distributions. The final distributions are Gaussian, and as such, the 50th percentiles of each distribution are taken for the luminosity bin centers and $\phi(L, z)$ points for each $\log L$ and z bin.

The uncertainties on the luminosity function points are measured by combining in quadrature the 1σ standard deviation of the aforementioned distributions and the error obtained by weighting each galaxy contribution to the V_{max} , following Marshall (1985):

$$\sigma(L, z) = \frac{1}{\Delta \log L} \sqrt{\sum_i \frac{1}{V_{\text{max}}^2}} \quad (10)$$

In this way, we account for the photometric uncertainties, although the fact that just a quarter of the sample has photo- z and the large chosen redshift bins reduces the impact of these errors for most of the LF points, accounting for $\sim 10\%$ of the total error budget. Whenever there are fewer than five sources per luminosity bin, the uncertainty on the data point is calculated from the confidence intervals reported in Gehrels (1986) for small number Poisson statistics. In these cases, $\sigma(L, z) = \phi \times \sigma_N/N$.

The final LFs and their uncertainties are listed in Table 2 and are reported as red dots in Figure 9.

We fit the measured radio luminosity functions $\phi(L, z)$ in each redshift bin with a modified Schechter function (Saunders et al. 1990),

$$\phi_0(L) = \phi_* \left(\frac{L}{L_*} \right)^{1-\alpha} \exp \left[-\frac{1}{2\sigma^2} \log^2 \left(1 + \frac{L}{L_*} \right) \right], \quad (11)$$

which behaves as a power-law function for luminosities below the turnover L_* and as a lognormal distribution for $L > L_*$. This is a function of four parameters, α being the faint-end power-law index, and σ is determined by the bright end, L_* is the turnover-luminosity knee where the function behavior changes, and ϕ_* is the normalization. A modified Schechter is a typical assumption for the radio and IR luminosity function (i.e., Saunders et al. 1990; Novak et al. 2017; Gruppioni et al. 2020), accounting for more objects in the bright-end part of the function than a normal Schechter function.

We assume that the shape of the LF does not change with cosmic time, and as such, we fix the shape parameters α and σ , and measure L_* and ϕ_* . The bright-end parameter σ is fixed at 0.63, as in Novak et al. (2017), where the authors infer the shape of the local LF from a sample of three radio surveys in the local universe (Condon et al. 2002; Best et al. 2005; Mauch & Sadler 2007). Given the depth of the radio observations upon which our sample is based, we are able to probe the faint-end part of the LF only in the first redshift bin. As such, we evaluate the faint-end α in the lowest- z bin, and keep that measured value fixed for the other redshift bins.

Parameter space exploration, looking for the best-fit parameters, is performed with ULTRANEST¹² (Buchner 2021), a Python module implementing importance nested-sampling Monte Carlo algorithm MLFriends (Buchner et al. 2014; Buchner 2019). We assume flat priors for all the free parameters in the ranges $\log L_*$: [19, 25], $\log \phi_*$: [-5, -1], α : [0, 3].

The measured luminosity functions and best-fit analytical forms are shown in Figure 9, where we also report the Novak et al. (2017) results in the closer redshift bin for comparison. LF values and best-fit parameters are reported in Tables 2–3.

For all the redshift bins, our LF reaches fainter luminosities by ~ 0.2 dex than those in Novak et al. (2017), while they sample the bright-end part better. The Novak et al. (2017) sample is derived from a wider area of 2 deg² in COSMOS, containing a factor ~ 10 more sources than our sample, which translates into LF points with smaller error bars, and access to brighter sources. The two LFs are in good agreement within the errors, with the notable exception of the bin $0.4 < z < 0.7$, where we obtain higher values at all luminosities, a difference that could be due to cosmic variance, i.e., an excess of galaxies in the redshift range corresponding to the bin. Our LF is in agreement also with the radio LF derived by Bonato et al. (2021), with LOFAR at 150 MHz, converted to 1.4 GHz assuming $\alpha = -0.7$.

5. The Cosmic Star Formation History

We derive the time evolution of the SFR density integrating, at different redshifts, the product between $\phi(L, z)$ and $SFR(L)$, i.e., the SFR corresponding to a given radio luminosity L :

$$SFRD(z) = \int_{L_{\min}}^{L_{\max}} \phi(L, z) \times SFR(L) d \log L. \quad (12)$$

Assuming that our LF can be extrapolated at luminosities lower and higher than the actually sampled LF, we integrate over the entire luminosity range (i.e., $L_{\min} = 0$ and $L_{\max} \rightarrow \infty$). The most consistent contribution to the integral comes from points located near the function knee L_* , as the integral rapidly

Table 2
Luminosity Function from the $1/V_{\max}$ Method

Redshift	$\log L_{1.4 \text{ GHz}}$ [WHz^{-1}]	$\log \phi$ [$\text{Mpc}^{-3} \text{dex}^{-1}$]
$0.1 < z < 0.4$	21.48 ± 0.02	$-2.40^{+0.26}_{-0.70}$
	21.99 ± 0.01	$-2.77^{+0.14}_{-0.14}$
	22.42 ± 0.01	$-3.20^{+0.25}_{-0.73}$
	22.84 ± 0.01	$-3.42^{+0.20}_{-0.87}$
$0.4 < z < 0.7$	22.16 ± 0.03	$-2.38^{+0.17}_{-0.17}$
	22.55 ± 0.00	$-2.75^{+0.07}_{-0.07}$
	22.96 ± 0.01	$-3.19^{+0.12}_{-0.12}$
	23.38 ± 0.02	$-3.80^{+0.20}_{-0.87}$
$0.7 < z < 1.0$	22.58 ± 0.03	$-2.54^{+0.15}_{-0.12}$
	22.88 ± 0.00	$-2.84^{+0.08}_{-0.07}$
	23.26 ± 0.01	$-3.19^{+0.09}_{-0.09}$
	23.63 ± 0.01	$-3.99^{+0.20}_{-0.87}$
$1.0 < z < 2.0$	23.04 ± 0.06	$-2.48^{+0.16}_{-0.15}$
	23.57 ± 0.01	$-3.55^{+0.07}_{-0.08}$
	23.96 ± 0.03	$-4.16^{+0.14}_{-0.13}$
	24.35 ± 0.06	$-4.72^{+0.20}_{-0.87}$
$2.0 < z < 3.0$	23.59 ± 0.03	$-2.94^{+0.28}_{-0.31}$
	23.94 ± 0.00	$-3.72^{+0.09}_{-0.11}$
	24.27 ± 0.01	$-4.26^{+0.14}_{-0.16}$
	24.60 ± 0.01	$-4.81^{+0.20}_{-0.87}$
$3.0 < z < 5.2$	23.70 ± 0.05	$-3.26^{+0.26}_{-0.70}$
	24.09 ± 0.03	$-3.98^{+0.26}_{-0.70}$
	24.27 ± 0.03	$-4.52^{+0.26}_{-0.70}$
	24.69 ± 0.01	$-4.98^{+0.26}_{-0.70}$

Table 3

ULTRANEST Best-fit Parameters to the Measured Luminosity Function with the Modified Schechter Function in Equation (11)

Redshift	α	$\log L_*$ (WHz^{-1})	$\log \phi_*$ ($\text{Mpc}^{-3} \text{dex}^{-1}$)
$0.1 < z < 0.4$	$1.62^{+0.56}_{-0.30}$	$22.31^{+1.19}_{-1.05}$	$-2.95^{+0.71}_{-0.74}$
$0.4 < z < 0.7$		$22.30^{+0.98}_{-0.33}$	$-2.49^{+0.33}_{-0.70}$
$0.7 < z < 1.0$		$22.61^{+0.59}_{-0.28}$	$-2.53^{+0.29}_{-0.49}$
$1.0 < z < 2.0$		$22.51^{+0.18}_{-0.12}$	$-2.16^{+0.21}_{-0.28}$
$2.0 < z < 3.0$		$23.04^{+0.33}_{-0.28}$	$-2.64^{+0.47}_{-0.46}$
$3.0 < z < 5.2$		$23.10^{+0.30}_{-0.25}$	$-2.75^{+0.44}_{-0.50}$

Note. α is measured in the first redshift bin, and fixed otherwise. σ is fixed to 0.63.

converges for higher luminosities. As such, the most reliable $SFRD$ measures will be those where the knee is well sampled, while for the rest, there will be a certain degree of uncertainty due to the fitted extrapolation (this is well visible in Figure 8 of Novak et al. 2017).

The IR emission is directly related to the SFR of a source due to its nature as reprocessed light coming from UV photons of newborn stars and reemitted at longer wavelengths (Kennicutt 1998; Kennicutt & Evans 2012)¹³

$$SFR[M_{\odot} \text{yr}^{-1}] = 2.84 \times 10^{-44} L_{\text{IR}}[\text{erg s}^{-1}]. \quad (13)$$

¹² <https://johannesbuchner.github.io/UltraNest/>

¹³ Rescaled for a Chabrier IMF.

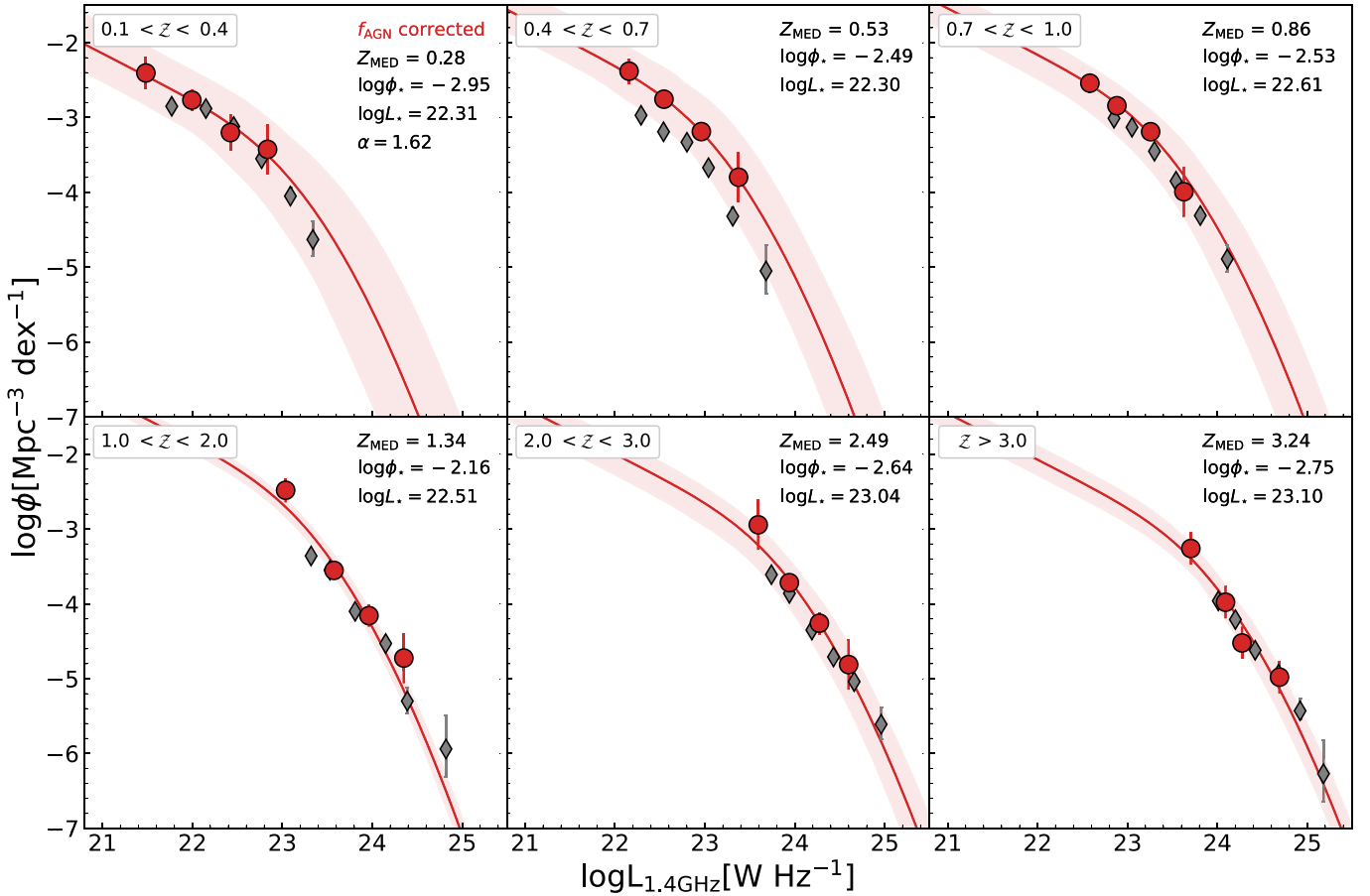


Figure 9. The 1.4 GHz luminosity function. Red circles are the measured ϕ luminosity function, while the line and shaded area are the best-fit and 1σ curves, respectively. Gray diamonds are from Novak et al. (2017).

Table 4
Star Formation Rate Density Values

Redshift	From ϕ
$0.1 < z < 0.4$	-1.78 ± 0.24
$0.4 < z < 0.7$	-1.38 ± 0.14
$0.7 < z < 1.0$	-1.16 ± 0.16
$1.0 < z < 2.0$	-0.96 ± 0.17
$2.0 < z < 3.0$	-0.99 ± 0.22
$z > 3.0$	-1.09 ± 0.25
$z > 3.0$ (incl. all H -dark)	-0.99 ± 0.32
H -dark with photo- z	$[-2.47; -1.69]$
All H -dark	$[-2.35; -1.58]$

Note. At $z > 3$, we report also the value obtained by adding to the sample the seven H -dark sources with high fidelity, but no photo- z , under the assumption that they all lie at $z \sim 3$. In the last two lines we report the values for the H -dark galaxies alone, first considering only those with a measured photo- $z > 3$, then including also the seven sources with no photo- z . We report our confidence intervals, where the lower limit is derived by summing the (observed) volume-weighted SFRs, and the upper limit is derived from ϕ .

As such, there is a direct link between the radio luminosity and the SFR via the IRRC,

$$SFR(L)[M_{\odot} \text{ yr}^{-1}] = 10^{q_{\text{TIR}}(z)} L_{1.4\text{GHz}} \times 10^{-24} [W \text{ Hz}^{-1}], \quad (14)$$

with $q_{\text{TIR}}(z)$ the relation obtained in Section 4.2.

This relation holds in the redshift interval of our interest, while it may start to break down at higher redshifts ($z > 6$), when the energy densities of the cosmic microwave background and the galactic magnetic field are similar, resulting in Compton cooling on the CMB from the accelerated electrons, thus leading to an underestimation of the SFR (Barger et al. 2014). By passing through the IRRC, we are able to decompose the FIR emission in its star formation and AGN components, and derive the SFR accordingly, something that it is not possible when directly dealing with the radio.

The evaluated $SFRD$ is reported in Table 4 and is shown in Figure 10, left panel, along with other estimates from the literature. At $z > 3$, we give a further estimate by adding to the sample the seven H -dark galaxies that have a high fidelity ($>90\%$), but no photometric redshift, under the assumption that they all lie at $z \sim 3$ and have the same luminosity distribution as the rest of the sample in the same redshift bin.

Our ϕ -inferred $SFRD$ follows the well-established cosmic picture of star formation depicted in Madau & Dickinson (2014) up to redshift ~ 1 . At earlier cosmic times, we obtain systematically higher values that are still compatible within the error bars, however, such as the two points at $z \sim 2.51$ and $z \sim 3.25$, up to a factor ~ 2 , resembling the (radio-inferred) evolution in Novak et al. (2017) and the (IR-inferred) evolution in Gruppioni et al. (2020). More recently, Malefahlo et al. (2022) report a decreasing radio-derived SFRD at high redshift, although the deviation with respect to our finding and the

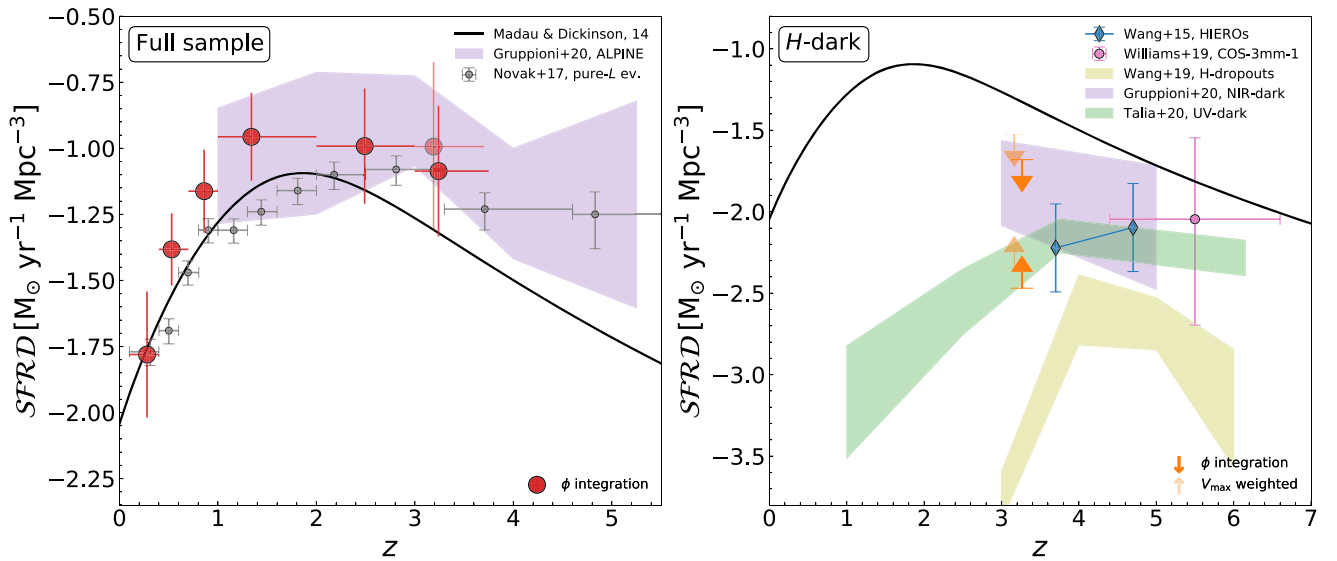


Figure 10. Left panel: the cosmic SFR density history for our sample of galaxies corrected per f_{AGN} (red points/arrows). The black curve is the best-fit function in Equation (15) of Madau & Dickinson (2014), scaled to a Chabrier IMF; the purple region is the $SFRD$ measured from 56 blindly selected sources in the ALPINE survey (Gruppioni et al. 2020); and gray points are the pure-luminosity evolution in Novak et al. (2017). Right panel: the same, limited to dark galaxies. All the values from the literature are V_{max} weighted. The green area is the $SFRD$ from a sample of radio-selected UV-dark galaxies in COSMOS (Talia et al. 2021), the yellow area is the $SFRD$ from the 39 ALMA-detected H -dropouts in Wang et al. (2019), blue diamonds represent a sample of high- z JH-blue HIEROs (Wang et al. 2016), the magenta circle corresponds to an NIR-dark galaxy serendipitously detected in COSMOS (Williams et al. 2019; Zavala 2021), and the purple region marks the subsample of NIR-dark galaxies in the ALPINE fields (Gruppioni et al. 2020). In both panels, the light red/orange points and arrows at $z > 3$ refer to the case in which we place all high-fidelity H -dark galaxies without a photometric redshift at $z \sim 3$.

finding of Novak et al. (2017) is likely a result of incompleteness due to their stellar mass selection, which also causes them to miss heavily obscured objects that still emit a significant amount of radio emission due to ongoing star formation, as the authors themselves point out in their conclusions. There are not enough sources at $z > 4$ in our sample to measure the $SFRD$ from the LF.

In general, our $SFRD$ values are higher than those in Novak et al. (2017; gray points in Figure 10), due to a combination of cosmic variance (i.e., the point at $z \sim 0.53$) and a steeper faint-end slope of the LF (1.62 versus 1.22).

5.1. Weighting the H -dark Contribution

We also evaluate separately the contributions of the H -dark galaxies to the SFRD. Since all but one of them with a photometric redshift are at $z \geq 3$, we focus only on that bin.

We evaluate the LF of both the sample of H -dark galaxies with a measured photo- z and the total sample of H -dark galaxies, assuming that those with no photo- z lie at $z \sim 3$, similarly to what was done for the full radio sample. Then, we integrate the LF to obtain the SFRD. Such a measurement is inevitably affected by the small number of sources. We fix the turnover luminosity to the luminosity measured with the full radio sample in the same redshift bin, and just fit the normalization ϕ_* , obtaining the H -dark contribution as the ratio of the two.

The assumption of an identical shape for the LF of H -dark galaxies and that of the full sample might bias the results. In principle, the fraction of highly obscured H -dark galaxies at lower SFR is expected to be smaller than for the full population. Therefore, the ϕ inferred points should be considered as upper limits to the $SFRD$.

Following Talia et al. (2021), we also derive an estimate of the $SFRD$ by summing the observed SFR of each galaxy,

weighted by its V_{max} , via a bootstrap analysis that takes into account the uncertainties on photometric redshift and L_{IR} . In this way, we actually obtain a lower limit to the SFRD.

The results from both methods are reported in the second part of Table 4 and in the right panel of Figure 10, along with a compilation of estimates coming from literature studies of extremely obscured galaxies in the NIR.

As we briefly mentioned in the introduction, there are multiple definitions for dark sources in the literature. Frequently used labels (HST-, UV-, OIR-, NIR-, and H -dark galaxies) refer to the fact that a common feature of these sources is that they are invisible or extremely faint at optical and/or NIR wavelengths, corresponding to the UV rest frame as most of these galaxies are supposedly extremely dust-obscured objects at high redshift. Such labels are obviously not absolute definitions, but they are relative to the depth of the specific band used for the selection in a given field. This inhomogeneity makes it quite challenging to compare different samples, although by now various works have shown that dark galaxies likely play an important role in the SFRD and mass assembly in the high-redshift universe. The comparison shown in the right panel of Figure 10 should be read keeping this caveat in mind.

Given our derived upper and lower limits for the SFRD of H -dark galaxies, we find that at $z \sim 3$, they account for between $\sim 3\%$ and $\sim 25\%$ of the total star formation activity with respect to the full radio sample, and between $\sim 7\%$ and $\sim 58\%$ with respect to the Madau & Dickinson (2014) estimate, which is based on UV-bright galaxies. A similar lower limit on the contribution of dark galaxies to the total SFRD at $z \sim 3$, as derived from UV-bright galaxies, is also reported by Talia et al. (2021) for a radio-selected sample in the COSMOS field and by Gruppioni et al. (2020) for a submillimeter sample in the ALPINE fields.

The space density of our H -dark galaxies at $z > 3$ is about $1.2 \times 10^{-5} \text{ Mpc}^{-3}$, in fair agreement with the numbers reported in previously cited works at the same redshift, e.g., $2.0 \times 10^{-5} \text{ Mpc}^{-3}$ (Wang et al. 2019) and $1.3 \times 10^{-5} \text{ Mpc}^{-3}$ (Talia et al. 2021). Existing semianalytical models (Henriques et al. 2015) and hydrodynamical simulations (Snyder et al. 2017; Pillepich et al. 2018) in the literature do not predict the early formation of such a large number of massive, dusty galaxies and underestimate their number density by one to two orders of magnitude (see also Wang et al. 2019) with respect to our findings.

6. Summary

In this work, we exploited a sample of radio-selected galaxies in deep 1.4 GHz VLA observations of the GOODS-N field to build the radio luminosity function and measure the cosmic evolution of the SFR density up to $z \sim 3.5$. There is a tension at redshift higher than 2 between the steep decline in SFRD that UV-based samples (i.e., LBGs) show and the rather flat trend derived from FIR/radio surveys. The latter are crucial to overcome the intrinsic limits of UV-based selections, i.e., poorly constrained dust correction at high z , extremely dusty undetected objects.

We start from the 1.4 GHz map and catalog of Owen (2018), combined with ancillary multiwavelength data, and select 554 radio sources with a counterpart in the F160W catalog (Barro et al. 2019), plus 17 H -dark galaxies. We are able to assign a redshift, either spectroscopic or photometric, to all our galaxies, except for nine H -dark sources.

We build the radio luminosity function after subtracting the AGN contamination from the radio emission. In particular, instead of altogether removing the sources with some evidence of nuclear activity from their radio excess, we estimate the fraction of AGN emission at 1.4 GHz and correct the fluxes accordingly. We fit the radio LF in five redshift bins with a modified Schechter function, assuming an invariant shape for the functional form, and measure the SFRD from the integration of the LF.

Our main finding is the evolution with redshift of the radio-inferred SFRD, which increases up to $z \sim 2$ and flattens at higher redshift. This result is consistent with other claims in the literature both from radio (Novak et al. 2017) and submillimeter (Gruppioni et al. 2020) surveys, and it confirms the tension at $z > 3$, already reported in previous works, with

respect to the SFRD estimates based on LBG samples (e.g., Madau & Dickinson 2014).

We also derive the SFRD of the subsample of H -dark galaxies at $z \sim 3$, and we estimate them to have a contribution to the total SFRD of 3%–25% and 7%–58% when considering the radio-based or the UV-based estimates, respectively. This result, which is consistent with other works that analyzed different samples of dark galaxies, highlights the possibly preeminent role that extremely obscured sources might play at high redshift. Dedicated follow-ups of such objects, with facilities such as ALMA and the James Webb Space Telescope (JWST), would allow a robust determination of their redshift and a proper characterization of their physical properties and evolution with cosmic time.

We thank the anonymous reviewer for their comments that improved the work quality and flow. We thank Frazer Owen and Lennox Cowie for kindly providing the JVLA 1.4 GHz and the SCUBA-2 850 μm maps, respectively, that we used throughout the work. We acknowledge the support from grant PRIN MIUR 2017-20173ML3WW_001. The National Radio Astronomy Observatory is a facility of the National Science Foundation operated under cooperative agreement by Associated Universities, Inc. This work has made use of the Rainbow Cosmological Surveys Database, which is operated by the Universidad Complutense de Madrid (UCM), partnered with the University of California Observatories at Santa Cruz (UCO/Lick, UCSC). We acknowledge the use of Python (v 3.7) libraries in the analysis. This research made use of Photutils, an Astropy package for the detection and photometry of astronomical sources (Bradley et al. 2019).

Facilities: VLA, HST, Spitzer, Herschel, CFHT, KPNO.

Software: astropy (Astropy Collaboration et al. 2013), photutils (Bradley et al. 2019), TheTractor (Lang et al. 2016a, 2016b), magphys (da Cunha et al. 2015, 2015; Battisti et al. 2019), sed3fit (Berta et al. 2013), ultranest (Buchner et al. 2014; Buchner 2019).

Appendix Spectral Energy Distributions of H -dark Galaxies

In this appendix we show the photometric data plus best-fit SEDs of the eight H -dark galaxies in our sample for which we were able to derive a photometric redshift (Figure 11).

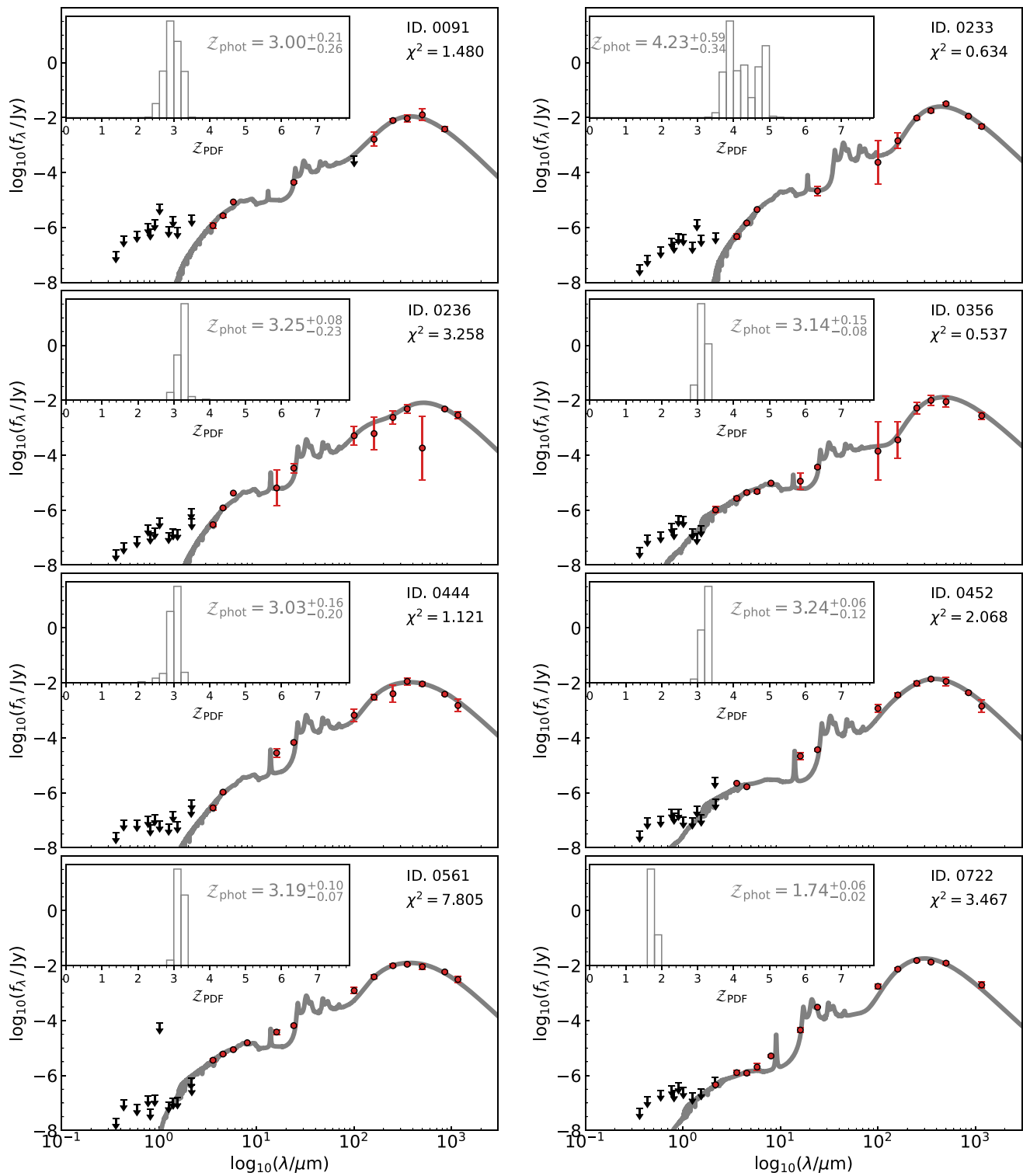



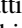
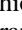
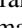
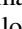
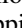


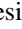
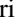




Figure 11. Best-fit SEDs (gray) of the H -dark sources in our radio-selected sample; red circles indicate the photometric measurements, and black arrows stand for upper limits. The redshift probability distribution function is also shown in the inset. We also report the reduced χ^2 .

ORCID iDs

Andrea Enia  <https://orcid.org/0000-0002-0200-2857>
 Margherita Talia  <https://orcid.org/0000-0003-4352-2063>
 Francesca Pozzi  <https://orcid.org/0000-0002-7412-647X>
 Andrea Cimatti  <https://orcid.org/0000-0002-4409-5633>
 Ivan Delvecchio  <https://orcid.org/0000-0001-8706-2252>
 Gianni Zamorani  <https://orcid.org/0000-0002-2318-301X>
 Quirino D'Amato  <https://orcid.org/0000-0002-9948-0897>
 Laura Bisigello  <https://orcid.org/0000-0003-0492-4924>
 Carlotta Gruppioni  <https://orcid.org/0000-0002-5836-4056>
 Giulia Rodighiero  <https://orcid.org/0000-0002-9415-2296>
 Francesco Calura  <https://orcid.org/0000-0002-6175-0871>
 Daniele Dallacasa  <https://orcid.org/0000-0003-1246-6492>
 Marika Giulietti  <https://orcid.org/0000-0002-1847-4496>
 Luigi Barchiesi  <https://orcid.org/0000-0003-3419-538X>
 Meriem Behiri  <https://orcid.org/0000-0002-6444-8547>
 Michael Romano  <https://orcid.org/0000-0002-9948-3916>

References

- Ashby, M. L. N., Willner, S. P., Fazio, G. G., et al. 2013, *ApJ*, 769, 80
 Ashby, M. L. N., Willner, S. P., Fazio, G. G., et al. 2015, *ApJS*, 218, 33
 Astropy Collaboration, Robitaille, T. P., Tollerud, E. J., et al. 2013, *A&A*, 558, A33
 Barger, A. J., Cowie, L. L., & Wang, W. H. 2008, *ApJ*, 689, 687
 Barger, A. J., Cowie, L. L., Chen, C. C., et al. 2014, *ApJ*, 784, 9
 Barro, G., Pérez-González, P. G., Cava, A., et al. 2019, *ApJS*, 243, 22
 Battisti, A. J., da Cunha, E., Grasha, K., et al. 2019, *ApJ*, 882, 61
 Berta, S., Magnelli, B., Nordon, R., et al. 2011, *A&A*, 532, A49
 Berta, S., Lutz, D., Santini, P., et al. 2013, *A&A*, 551, A100
 Bertin, E., & Arnouts, S. 1996, *A&AS*, 117, 393
 Best, P. N., Kauffmann, G., Heckman, T. M., & Ivezić, Ž. 2005, *MNRAS*, 362, 9
 Béthermin, M., Fudamoto, Y., Ginolfi, M., et al. 2020, *A&A*, 643, A2
 Bonato, M., Prandoni, I., De Zotti, G., et al. 2021, *A&A*, 656, A48
 Bonzini, M., Mainieri, V., Padovani, P., et al. 2015, *MNRAS*, 453, 1079
 Bouwens, R. J., Illingworth, G. D., Oesch, P. A., et al. 2015, *ApJ*, 803, 34
 Boyle, B. J., & Terlevich, R. J. 1998, *MNRAS*, 293, L49
 Bradley, L., Sipőcz, B., Robitaille, T., et al. 2019, *astropy/photutils: v0.7.2*, v0.7.2, Zenodo, doi: 10.5281/zenodo.3568287
 Bruzual, G., & Charlot, S. 2003, *MNRAS*, 344, 1000
 Buchner, J. 2019, *PASP*, 131, 108005
 Buchner, J. 2021, *JOSS*, 6, 3001
 Buchner, J., Georgakakis, A., Nandra, K., et al. 2014, *A&A*, 564, A125
 Casey, C. M., Scoville, N. Z., Sanders, D. B., et al. 2014, *ApJ*, 796, 95
 Casey, C. M., Zavala, J. A., Manning, S. M., et al. 2021, *ApJ*, 923, 215
 Ceraj, L., Smolčić, V., Delvecchio, I., et al. 2018, *A&A*, 620, A192
 Chabrier, G. 2003, *PASP*, 115, 763
 Charlot, S., & Fall, S. M. 2000, *ApJ*, 539, 718
 Ciliegi, P., Zamorani, G., Hasinger, G., et al. 2003, *A&A*, 398, 901
 Ciliegi, P., Jurlin, N., Butler, A., et al. 2018, *A&A*, 620, A11
 Condon, J. J. 1992, *ARA&A*, 30, 575
 Condon, J. J., Cotton, W. D., & Broderick, J. J. 2002, *AJ*, 124, 675
 Condon, J. J., Helou, G., Sanders, D. B., & Soifer, B. T. 1993, *AJ*, 105, 1730
 Cowie, L. L., Barger, A. J., Hsu, L. Y., et al. 2017, *ApJ*, 837, 139
 da Cunha, E., Charlot, S., & Elbaz, D. 2008, *MNRAS*, 388, 1595
 da Cunha, E., Walter, F., Smail, I. R., et al. 2015, *ApJ*, 806, 110
 Daddi, E., Dannerbauer, H., Liu, D., et al. 2015, *A&A*, 577, A46
 de Jong, T., Klein, U., Wielebinski, R., & Wunderlich, E. 1985, *A&A*, 147, L6
 Decarli, R., Walter, F., Carilli, C., et al. 2014, *ApJ*, 782, 78
 Decarli, R., Walter, F., Aravena, M., et al. 2016, *ApJ*, 833, 69
 Decarli, R., Walter, F., González-López, J., et al. 2019, *ApJ*, 882, 138
 Del Moro, A., Alexander, D. M., Mullaney, J. R., et al. 2013, *A&A*, 549, A59
 Delhaize, J., Smolčić, V., Delvecchio, I., et al. 2017, *A&A*, 602, A4
 Delvecchio, I., Gruppioni, C., Pozzi, F., et al. 2014, *MNRAS*, 439, 2736
 Delvecchio, I., Smolčić, V., Zamorani, G., et al. 2017, *A&A*, 602, A3
 Delvecchio, I., Daddi, E., Sargent, M. T., et al. 2021, *A&A*, 647, A123
 Dickinson, M., Giavalisco, M., & GOODS Team 2003a, in *ESO Symp.*, The Mass of Galaxies at Low and High Redshift, ed. R. Bender & A. Renzini (Berlin: Springer), 324
 Dickinson, M., Bergeron, J., Casertano, S., et al. 2003b, *Great Observatories Origins Deep Survey (GOODS) Validation Observations, Spitzer Proposal 196*
 Donley, J. L., Rieke, G. H., Rigby, J. R., & Pérez-González, P. G. 2005, *ApJ*, 634, 169
 Dunlop, J. S., McLure, R. J., Biggs, A. D., et al. 2017, *MNRAS*, 466, 861
 Faisst, A. L., Schaerer, D., Lemaux, B. C., et al. 2020, *ApJS*, 247, 61
 Feltre, A., Hatziminaoglou, E., Fritz, J., & Franceschini, A. 2012, *MNRAS*, 426, 120
 Franco, M., Elbaz, D., Béthermin, M., et al. 2018, *A&A*, 620, A152
 Gehrels, N. 1986, *ApJ*, 303, 336
 Giavalisco, M., Ferguson, H. C., Koekemoer, A. M., et al. 2004, *ApJL*, 600, L93
 González-López, J., Novak, M., Decarli, R., et al. 2020, *ApJ*, 897, 91
 Grogin, N. A., Kocevski, D. D., Faber, S. M., et al. 2011, *ApJS*, 197, 35
 Gruppioni, C., Pozzi, F., Rodighiero, G., et al. 2013, *MNRAS*, 432, 23
 Gruppioni, C., Béthermin, M., Loiacono, F., et al. 2020, *A&A*, 643, A8
 Guidetti, D., Bondi, M., Prandoni, I., et al. 2017, *MNRAS*, 471, 210
 Hatsukade, B., Kohno, K., Yamaguchi, Y., et al. 2018, *PASJ*, 70, 105
 Helou, G., Soifer, B. T., & Rowan-Robinson, M. 1985, *ApJL*, 298, L7
 Henriques, B. M. B., White, S. D. M., Thomas, P. A., et al. 2015, *MNRAS*, 451, 2663
 Holland, W. S., Robson, E. I., Gear, W. K., et al. 1999, *MNRAS*, 303, 659
 Hsu, L.-T., Lin, L., Dickinson, M., et al. 2019, *ApJ*, 871, 233
 Hughes, D. H., Serjeant, S., Dunlop, J., et al. 1998, *Natur*, 394, 241
 Ishigaki, M., Kawamata, R., Ouchi, M., et al. 2018, *ApJ*, 854, 73
 Kajisawa, M., Ichikawa, T., Tanaka, I., et al. 2011, *PASJ*, 63, 379
 Kennicutt, R. C. 1998, *ARA&A*, 36, 189
 Kennicutt, R. C., & Evans, N. J. 2012, *ARA&A*, 50, 531
 Koekemoer, A. M., Faber, S. M., Ferguson, H. C., et al. 2011, *ApJS*, 197, 36
 Lang, D., Hogg, D. W., & Mykytyn, D. 2016a, *The Tractor: Probabilistic astronomical source detection and measurement*, *Astrophysics Source Code Library*, ascl:1604.008
 Lang, D., Hogg, D. W., & Schlegel, D. J. 2016b, *AJ*, 151, 36
 Le Fèvre, O., Béthermin, M., Faisst, A., et al. 2020, *A&A*, 643, A1
 Liu, D., Daddi, E., Dickinson, M., et al. 2018, *ApJ*, 853, 172
 Lutz, D., Poglitsch, A., Altieri, B., et al. 2011, *A&A*, 532, A90
 Madau, P., & Dickinson, M. 2014, *ARA&A*, 52, 415
 Magnelli, B., Popesso, P., Berta, S., et al. 2013, *A&A*, 553, A132
 Magnelli, B., Karim, A., Staguhn, J., et al. 2019, *ApJ*, 877, 45
 Malefahlo, E. D., Jarvis, M. J., Santos, M. G., et al. 2022, *MNRAS*, 509, 4291
 Manning, S. M., Casey, C. M., Zavala, J. A., et al. 2021, *ApJ*, 925, 23
 Marshall, H. L. 1985, *ApJ*, 299, 109
 Mauch, T., & Sadler, E. M. 2007, *MNRAS*, 375, 931
 McLeod, D. J., McLure, R. J., & Dunlop, J. S. 2016, *MNRAS*, 459, 3812
 Molnar, D. C., Sargent, M. T., Leslie, S., et al. 2021, *MNRAS*, 504, 118
 Murphy, E. J. 2013, *ApJ*, 777, 58
 Murphy, E. J., Momjian, E., Condon, J. J., et al. 2017, *ApJ*, 839, 35
 Novak, M., Smolčić, V., Delhaize, J., et al. 2017, *A&A*, 602, A5
 Oesch, P. A., Bouwens, R. J., Illingworth, G. D., Labbé, I., & Stefanon, M. 2018, *ApJ*, 855, 105
 Oliver, S. J., Bock, J., Altieri, B., et al. 2012, *MNRAS*, 424, 1614
 Owen, F. N. 2018, *ApJS*, 235, 34
 Pérez-González, P. G., Rieke, G. H., Egami, E., et al. 2005, *ApJ*, 630, 82
 Pérez-González, P. G., Cava, A., Barro, G., et al. 2013, *ApJ*, 762, 46
 Pillepich, A., Springel, V., Nelson, D., et al. 2018, *MNRAS*, 473, 4077
 Planck Collaboration, Ade, P. A. R., Aghanim, N., et al. 2016, *A&A*, 594, A13
 Retana-Montenegro, E., Röttgering, H. J. A., Shimwell, T. W., et al. 2018, *A&A*, 620, A74
 Riechers, D. A., Boogaard, L. A., Decarli, R., et al. 2020, *ApJL*, 896, L21
 Rowan-Robinson, M., Oliver, S., Wang, L., et al. 2016, *MNRAS*, 461, 1100
 Saunders, W., Rowan-Robinson, M., Lawrence, A., et al. 1990, *MNRAS*, 242, 318
 Schmidt, M. 1968, *ApJ*, 151, 393
 Smolčić, V., Novak, M., Bondi, M., et al. 2017, *A&A*, 602, A1
 Snyder, G. F., Lotz, J. M., Rodriguez-Gomez, V., et al. 2017, *MNRAS*, 468, 207
 Sutherland, W., & Saunders, W. 1992, *MNRAS*, 259, 413
 Talia, M., Cimatti, A., Giulietti, M., et al. 2021, *ApJ*, 909, 23
 van der Kruit, P. C. 1971, *A&A*, 15, 110
 Walter, F., Decarli, R., Aravena, M., et al. 2016, *ApJ*, 833, 67

- Wang, T., Elbaz, D., Schreiber, C., et al. 2016, [ApJ](#), 816, 84
Wang, T., Schreiber, C., Elbaz, D., et al. 2019, [Natur](#), 572, 211
Wang, W.-H., Cowie, L. L., Barger, A. J., Keenan, R. C., & Ting, H.-C. 2010, [ApJS](#), 187, 251
Weaver, J. R., Kauffmann, O. B., Ilbert, O., et al. 2022, [ApJS](#), 258, 11
Williams, C. C., Labbe, I., Spilker, J., et al. 2019, [ApJ](#), 884, 154
Williams, R. E., Blacker, B., Dickinson, M., et al. 1996, [AJ](#), 112, 1335
Yamaguchi, Y., Kohno, K., Hatsukade, B., et al. 2019, [ApJ](#), 878, 73
Yun, M. S., Reddy, N. A., & Condon, J. J. 2001, [ApJ](#), 554, 803
Zavala, J. A. 2021, [RNAAS](#), 5, 15